UC Berkeley
UC Berkeley Previously Published Works

Title
A flexible organic reflectance oximeter array

Permalink
https://escholarship.org/uc/item/7wv7q14t

Journal
Proceedings of the National Academy of Sciences of the United States of America, 115(47)

ISSN
0027-8424

Authors
Khan, Yasser
Han, Donggeon
Pierre, Adrien
et al.

Publication Date
2018-11-20

DOI
10.1073/pnas.1813053115

Peer reviewed

A flexible organic reflectance oximeter array

Yasser Khan[a,1], Donggeon Han[a], Adrien Pierre[a], Jonathan Ting[a], Xingchun Wang[a], Claire M. Lochner[a], Gianluca Bovo[b], Nir Yaacobi-Gross[b], Chris Newsome[b], Richard Wilson[b], and Ana C. Arias[a,1]

[a]Department of Electrical Engineering and Computer Sciences, University of California, Berkeley, CA 94720; and [b]Cambridge Display Technology Limited, Godmanchester, Cambridgeshire, PE29 2XG, United Kingdom

Transmission-mode pulse oximetry, the optical method for determining oxygen saturation in blood, is limited to only tissues that can be transilluminated, such as the earlobes and the fingers. The existing sensor configuration provides only single-point measurements, lacking 2D oxygenation mapping capability. Here, we demonstrate a flexible and printed sensor array composed of organic light-emitting diodes and organic photodiodes, which senses reflected light from tissue to determine the oxygen saturation. We use the reflectance oximeter array beyond the conventional sensing locations. The sensor is implemented to measure oxygen saturation on the forehead with 1.1% mean error and to create 2D oxygenation maps of adult forearms under pressure-cuff–induced ischemia. In addition, we present mathematical models to determine oxygenation in the presence and absence of a pulsatile arterial blood signal. The mechanical flexibility, 2D oxygenation mapping capability, and the ability to place the sensor in various locations make the reflectance oximeter array promising for medical sensing applications such as monitoring of real-time chronic medical conditions as well as postsurgery recovery management of tissues, organs, and wounds.

flexible electronics | wearable sensors | bioelectronics | organic electronics | oximetry

Hemoglobin, a protein molecule in the blood, transports oxygen from the lungs to the body's tissues. Oximeters determine oxygen saturation (SO_2) in tissues by optically quantifying the concentration of oxyhemoglobin (HbO_2) and deoxyhemoglobin (Hb) (1). Pulse oximetry, the most ubiquitous noninvasive method of oximetry, performs this ratiometric optical measurement on pulsatile arterial blood via photoplethysmography (PPG) at two different wavelengths (2). Pulse oximeters use optoelectronic sensors composed of light-emitting diodes (LEDs) and photodiodes (PDs) and operate at red and near-infrared (NIR) wavelengths, where the molar absorptivities of HbO_2 and Hb are significantly different. While both transmitted and reflected light can be used for pulse oximetry, in transmission-mode pulse oximetry ($S_pO_2^t$), the LEDs shine through the tissue and the transmitted light is collected using the PD on the opposite side (*SI Appendix, Fig. S1*)—this restricts sensing locations to only tissues that can be transilluminated, such as the earlobes and the fingers, and the feet for neonates. On the contrary, reflection-mode pulse oximetry ($S_pO_2^r$) uses LEDs and PDs on the same side of the tissue (*SI Appendix, Fig. S1*), which allows for diverse sensing locations, such as the forehead, forearm, abdomen, and leg. Additionally, $S_pO_2^r$ provides 2D oxygenation mapping capability with an array of sensors, whereas only single-point measurements can be performed with $S_pO_2^t$.

Recent progress in flexible and stretchable sensors has made them extremely promising for medical sensing and diagnostics because they enhance the signal-to-noise ratio (SNR) by establishing a conformal sensor–skin interface (3–11). Consequently, novel flexible sensors using organic and inorganic optoelectronics for transmission and reflection-mode pulse oximetry show a higher SNR due to a reduction in ambient noise (12–18).

Lochner et al. (17) demonstrated $S_pO_2^t$ on the finger using an all-organic optoelectronic sensor. Yokota et al. (13) demonstrated $S_pO_2^r$ on the fingertips using an ultraflexible photonic skin. Kim et al. (12) used a wireless optoelectronic system to monitor blood flow and tissue oxygenation. The focus and features of recently reported flexible oximeters are summarized in *SI Appendix, Table S1*. Noninvasive 2D oxygenation mapping capability has the potential to transform real-time and postsurgery management and monitoring of wounds, tissues, and organs (19–22). An in vivo spatial oxygenation mapping device can aid in assessing tissue damage and injury susceptibility. One such application scenario, where a flexible optoelectronic sensor array is used to map 2D oxygenation of a skin graft, is illustrated in Fig. 1*A*. To date, a flexible optoelectronic sensor capable of spatial mapping of oxygenation has not been demonstrated.

Here, we report a reflectance oximeter array (ROA), a flexible and printed electronic system realized by printing and integrating arrays of organic optoelectronics with conventional silicon integrated circuits for blood and tissue oximetry. The ROA is composed of four red and four NIR printed organic light-emitting diodes (OLEDs) and eight organic photodiodes (OPDs) (Fig. 1 *B* and *C*). We use red (612 nm) and NIR (725 nm) OLEDs, where the molar absorptivities of HbO_2 and Hb are

Significance

The optical method to determine oxygen saturation in blood is limited to only tissues that can be transilluminated. The status quo provides a single-point measurement and lacks 2D oxygenation mapping capability. We use organic printed optoelectronics in a flexible array configuration that senses reflected light from tissue. Our reflectance oximeter is used beyond conventional sensing locations and accurately measures oxygen saturation on the forehead. In a full system implementation, coupled with a mathematical model, we create 2D oxygenation maps of adult forearms under pressure-cuff–induced ischemia. Our skin-like flexible sensor system has the potential to transform oxygenation monitoring of tissues, wounds, skin grafts, and transplanted organs.

Fig. 1. Overview and operation of the printed reflectance oximeter array (ROA). (*A*) Schematic of an application scenario of the ROA: 2D oxygenation mapping of a skin graft on the forearm. After surgery, the ROA is placed on the skin graft to map oxygenation of the reconstructed skin. (*B*) ROA sensor configuration. Red and NIR OLED arrays composed of 2×2 pixels each are placed side by side, where the pixels are arranged in a checkerboard pattern. The OPD array composed of 8 pixels is placed on top of the OLED arrays. The OLEDs are used as light emitters: $I_0(\lambda)$ is the incident light intensity. OPDs are used to collect the diffused reflected light, $I(\lambda)$. The OLEDs and OPDs are spaced at d cm (emitter–detector spacing). $\mu_a(\lambda)$ is the absorption coefficient of the sensed tissue, which depends on the specific absorption coefficients and concentration of HbO_2 and Hb, and DPF is the differential pathlength factor. (*C*) Photo of the ROA on top of a person's forearm. (*D*) The molar extinction coefficients of HbO_2 and Hb and the ratio of the molar extinction coefficients of Hb and HbO_2. Three regions are shown: (*i*) green ($\varepsilon_{Hb}/\varepsilon_{HbO_2} < 2$), (*ii*) red ($\varepsilon_{Hb}/\varepsilon_{HbO_2} > 6$), and (*iii*) NIR ($\varepsilon_{Hb}/\varepsilon_{HbO_2} < 3$). Either of the combinations of "red and green" or "red and NIR" can be used for oximetry.

significantly different (Fig. 1*D*). The OPD and OLED arrays are fabricated on separate substrates and then assembled together to form the ROA (*SI Appendix*, Fig. S2). Since organic optoelectronics and printing techniques such as blade coating and screen printing are used to fabricate the sensor on flexible plastic substrates, the sensor array is comfortable to wear and increases the SNR by establishing a high-fidelity sensor–skin interface. We implement the reflectance oximeter to measure $S_pO_2^r$ on the forehead with 1.1% mean error compared with commercial transmission-mode pulse oximeters. In the case of a medical shock, low blood perfusion, or organ injury, the pulsatile arterial blood signal of PPG becomes too weak to be used for pulse oximetry (23). For the aforementioned cases and locations on the body with a low pulsatile PPG signal, we demonstrate a method to determine oxygenation in the absence of a pulsatile arterial blood signal. Also, the array implementation of the ROA allows us to create a 2D mapping of oxygenation of an area rather than a single point. By using the array, we spatially map oxygenation values of a volunteer's forearm under normal and ischemic conditions. In addition, we discuss the sensor design, signal requirements, sensor fabrication, and the measurement methodology of the ROA. We believe the tools and devices developed in this work can be used for medical sensing applications such as in vivo 2D mapping of oxygenation of tissues, wounds, skin grafts, or transplanted organs.

Results

Analytical Models for Reflectance Oximetry. Oximeters use the property that the molar extinction coefficients of Hb and HbO_2 vary appreciably over the visible and NIR spectrum. If two regions in the spectrum are chosen so that in one region, Hb has a higher absorptivity than HbO_2, and in the other region, Hb has a lower absorptivity than HbO_2, a ratiometric measurement can be performed to obtain the concentration of HbO_2 and Hb. The oxygen saturation, SO_2 is the concentration of HbO_2 divided by the sum of the concentrations of HbO_2 (C_{HbO_2}) and Hb (C_{Hb}): $SO_2 = \frac{C_{HbO_2}}{C_{HbO_2} + C_{Hb}}$. In Fig. 1*D*, three regions are shown: (*i*) green ($\varepsilon_{Hb}/\varepsilon_{HbO_2} < 2$), (*ii*) red ($\varepsilon_{Hb}/\varepsilon_{HbO_2} > 6$), and (*iii*) NIR ($\varepsilon_{Hb}/\varepsilon_{HbO_2} < 3$). Therefore, the combinations of red and green or red and NIR can be used for oximetry because of the contrast in molar extinction coefficients. Since the PPG signal magnitude for NIR is higher than the visible spectrum because light attenuation in tissue for NIR is much less than the visible spectrum, we use red and NIR OLEDs. In addition, the optical flux requirement for oximetry is less stringent for NIR than for visible colors—the NIR OLEDs used in the ROA provide 0.2 mW of flux, compared with the 0.9 mW of flux of the red OLEDs at the operating condition of 10 mA·cm^{-2} (*SI Appendix*, Fig. S3).

The operation of noninvasive reflectance oximetry can be grouped into two modes: (*i*) reflection-mode pulse oximetry

(SpO_2^r), when a pulsatile PPG signal is present, and (*ii*) reflectance oximetry, when a pulsatile PPG signal is absent. If a pulsatile PPG signal is present, a modified Beer–Lambert's law can be used to model the light propagation in tissue as shown in Fig. 1*B* and Eq. **1**,

$$I(\lambda) = I_0(\lambda)e^{-\mu_a \cdot (\lambda) \cdot d \cdot DPF(\lambda)}, \quad [1]$$

where $I(\lambda)$ is the measured diffused reflected light intensity, $I_0(\lambda)$ is the incident light intensity, $\mu_a(\lambda)$ is the absorption coefficient of the sensed tissue, d is the distance between the light emitter and detector, and $DPF(\lambda)$ is the differential pathlength factor (DPF), which accounts for the multiple scattering of light in tissue. The light attenuation in pulsatile arterial blood can be used to calculate $S_pO_2^r$ in accordance with Beer–Lambert's law and an empirical correction according to Eq. **2** (the complete derivation is provided in *SI Appendix*):

$$S_pO_2(R'_{os}) = \frac{\varepsilon_{\lambda_1,Hb} - \varepsilon_{\lambda_2,Hb}R'_{os}}{(\varepsilon_{\lambda_1,Hb} - \varepsilon_{\lambda_1,HbO_2}) + (\varepsilon_{\lambda_2,HbO_2} - \varepsilon_{\lambda_2,Hb})R'_{os}}. \quad [2]$$

Here, $\varepsilon_{\lambda,HbO_2}$ and $\varepsilon_{\lambda,Hb}$ are the molar extinction coefficients of oxyhemoglobin and deoxyhemoglobin at each wavelength. $R'_{os} = \frac{R_{os}}{\frac{DPF_{\lambda_1}}{DPF_{\lambda_2}}}$, where $R_{os} = \frac{AC_{\lambda_1}/DC_{\lambda_1}}{AC_{\lambda_2}/DC_{\lambda_2}}$, is the ratio of pulsatile (ac) to stationary (dc) signals at the two wavelengths.

In the case of low perfusion or in the absence of a pulsatile arterial blood signal, pulse oximetry in both transmission and reflection modes cannot be performed. In these scenarios, Eq. **1** can be rewritten to measure the time-varying light intensity attenuation, $\Delta I(\lambda)$ in blood and tissue. Here, $\Delta \mu_a$ expresses the change in absorption during the measurement:

$$\Delta I(\lambda) = I_0(\lambda)e^{-\Delta\mu_a \cdot (\lambda) \cdot d \cdot DPF(\lambda)}. \quad [3]$$

$\Delta \mu_a(\lambda)$ can be represented as the sum of the molar extinction coefficients multiplied by the concentrations of HbO_2 and Hb:

$$\Delta\mu_a(\lambda) = \varepsilon_{HbO_2}(\lambda) \cdot \Delta C_{HbO_2} + \varepsilon_{Hb}(\lambda) \cdot \Delta C_{Hb}. \quad [4]$$

Since there are two wavelength channels, a system of linear equations can be established using Eqs. **3** and **4**:

$$\begin{bmatrix} \varepsilon_{HbO_2}(\lambda_1) & \varepsilon_{Hb}(\lambda_1) \\ \varepsilon_{HbO_2}(\lambda_2) & \varepsilon_{Hb}(\lambda_2) \end{bmatrix} \cdot \begin{bmatrix} \Delta C_{HbO_2} \\ \Delta C_{Hb} \end{bmatrix} = \begin{bmatrix} \frac{\ln\frac{I_0(\lambda_1)}{\Delta I(\lambda_1)}}{d \cdot DPF(\lambda_1)} \\ \frac{\ln\frac{I_0(\lambda_2)}{\Delta I(\lambda_2)}}{d \cdot DPF(\lambda_2)} \end{bmatrix}. \quad [5]$$

In Eq. **5**, the molar extinction coefficients and $DPF(\lambda)$ can be obtained from the literature (1, 24). Since change in the concentration of HbO_2 (ΔC_{HbO_2}) and Hb (ΔC_{Hb}) can be calculated, the change in oxygen saturation (ΔSO_2) can be determined for the transient measurement. The complete derivation of Eq. **5** is provided in *SI Appendix*.

Reflectance Oximeter Design and Placement on the Body. Emitter–detector spacing (d) is an important design parameter for reflectance oximetry. To find the optimal d, we use a reflection-mode sensor board and measured the effect of d on PPG ac and dc signals at the eight locations on the body as depicted in *SI Appendix*, Fig. S4 *A and B*. The schematic of the sensor, containing three rings of four PDs spaced at 0.5 cm, 0.8 cm, and 1.1 cm away from the red and NIR LEDs at the center, is shown in *SI Appendix*, Fig. S4*C*. Both ac and dc signal magnitude drops exponentially with increasing d. *SI Appendix*, Fig. S4 *D and E* shows ac and dc signals for $d = 0.5$ cm, 0.8 cm, and

1.1 cm recorded on the wrist. When placed at $d < 0.5$ cm, the dc signal saturates the PD. This issue can be mitigated by putting an optical barrier between the LED and the PD to reduce direct coupling of light from the LED to the PD. While $d = 0.5$ cm provided us the best SNR, d can be different for other sensor designs. For a single-pixel reflectance sensor, a minimum optical flux should be maintained to resolve the pulsatile PPG signal. We measured that this minimum flux is ≈ 0.2 mW for NIR and ≈ 0.6 mW for red light. Once the minimum optical flux is ensured, the emitter–detector spacing (d) can be reduced so that the light detected from the arteries (signal) is distinguishable from the light scattered by the skin surface (noise). Overall, the optical flux output of the LEDs, external quantum efficiency (EQE) of the PD, and active area of the LEDs and the PD influence the optimum d for a reflection-mode sensor. All of the mentioned strategies for reducing d can be used for scaling down the pixel-to-pixel spacing of the ROA, which will reduce the array size while providing an adequate signal level to quantify the light absorption in blood and tissue.

An approach similar to obtaining the optimal d is used to find the optimal sensing location for SpO_2^r—we place the reflection-mode sensor at eight different locations on the body as depicted in *SI Appendix*, Fig. S4 *A* and *B*. *SI Appendix*, Fig. S4*A* shows the pulsatile (ac) signal magnitude for red (Red_{ac}) and NIR (NIR_{ac}) channels with an emitter–detector spacing, $d = 0.5$ cm. A high ac signal and a low dc signal are desirable for PPG measurements. The forehead provides the strongest peak–peak ac signal current, 20 nA for red and 60 nA for NIR, making it the most suitable location for SpO_2^r. The signal strength drops roughly by half on the wrists. Although we observed a clear degradation of the ac signal on the ribcage and the legs, heart rate and oxygenation values could be extracted from the measured signal. Similar to that for the ac signal, the forehead provides the highest dc signal, while the ribcage demonstrates the lowest dc signal magnitude. *SI Appendix*, Fig. S5 provides the full dataset of the ac and dc measurements at the eight sensing locations for five subjects. The reflectance sensor is mounted on the skin, using an adhesive foam dressing. The sensor mounting photos are shown in *SI Appendix*, Fig. S6.

OLED and OPD Array Fabrication and Characterization. We printed the organic optoelectronics of the ROA on separate substrates and then assembled them to form the sensor array. With 0.7 × 0.7 cm active area for both OLEDs and OPDs and 0.5 cm spacing between the OLEDs and OPDs, the dimension of the complete ROA is 4.3 cm in both length and width. The OLED arrays are fabricated on top of polyethylene naphthalate (PEN) substrates with patterned indium tin oxide (ITO) for contacts. A surface energy patterning (SEP) step is then performed that creates hydrophilic regions where poly(3,4-ethylenedioxythiophene)-poly(styrenesulfonate) (PEDOT:PSS) is blade coated, which is discussed in detail by Han et al. (15, 25) (Fig. 2*A*, *Left*). The interlayer and the emission layer are deposited using subsequent blade-coating steps (Fig. 2*B*, *Left*). Then, the dielectric and the silver traces are printed using a screen printer (Fig. 2*C*, *Left*). The purpose of printing the dielectric is to prevent shorts between the underlying ITO strips and the silver traces. Finally, thermal evaporation is used to deposit calcium/aluminum to finish the fabrication of OLED arrays (Fig. 2*D*, *Left*). Each OLED pixel is encapsulated with UV curable epoxy and a plastic film. The OLED device stack is shown in Fig. 2*G*. The same process steps apply for both red and NIR OLEDs; only the active materials are different.

The OPD array is fabricated on a planarized PEN substrate. A PEDOT:PSS anode is blade coated using the SEP technique as shown in Fig. 2*A*, *Right*. The SEP process for OPDs is
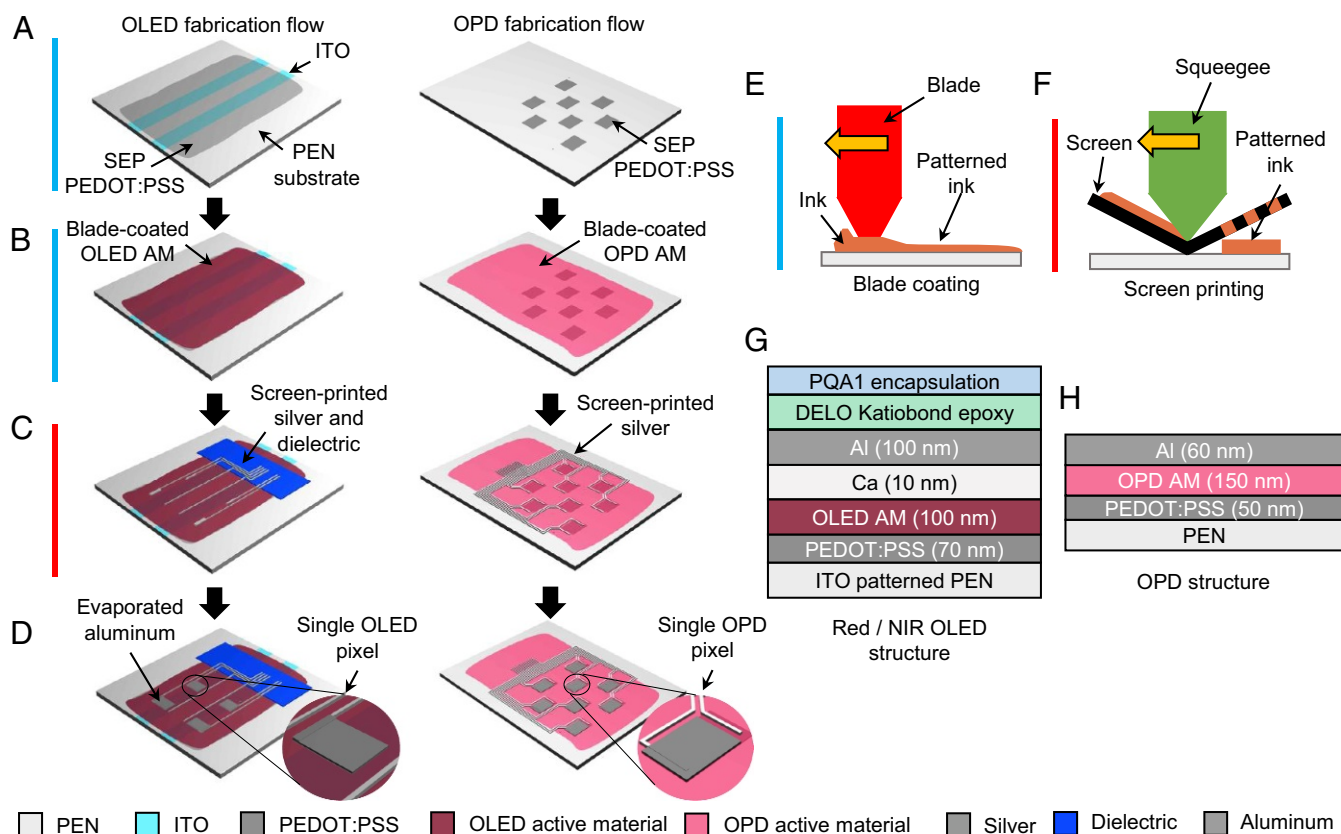
Fig. 2. Fabrication flow of the OLED and OPD arrays for the ROA. (*A–D*) The OLED and OPD array fabrication steps are shown side by side. For the OLED array, only one color consisting of 4 pixels is shown for simplicity—the same fabrication steps are used for red and NIR OLEDs. For the OPD array, the complete array consists of 8 pixels. (*A*) PEDOT:PSS is blade coated using surface energy patterning (SEP) on ITO-patterned PEN for the OLEDs and on a planarized PEN for the OPDs. (*B*) Active layers are blade coated—brick color indicates OLED active material and pink color indicates OPD active material. (*C*) Silver traces are screen printed on both OLEDs and OPDs. The OLEDs require an additional dielectric layer (blue) to prevent shorting of the anode to the cathode. (*D*) Aluminum cathode is evaporated, which defines the active area of the pixel. *D, Insets* show a zoomed-in view of the individual pixels. (*E* and *F*) The deposition techniques: Blade coating and screen printing are schematically shown and the color bars of the fabrication steps in *A–C, Left* indicate the deposition technique used for that respective layer: sky blue for blade coating and red for screen printing. (*G* and *H*) Device structure of the OLED and the OPD, respectively.

previously described by Pierre et al. (26, 27). A patterned anode is necessary because, without patterning, a large parasitic capacitance is formed between the PEDOT:PSS layer and the body, which obscures the signal in noise. The active layer is then blade coated (Fig. 2*B, Right*). Next, silver traces are screen printed to connect the anodes and cathodes of each pixel to external circuitry as shown in Fig. 2*C, Right*. Finally, an aluminum cathode is evaporated to complete the device stack, which is shown in Fig. 2*H*.

The OPD and OLED arrays are shown in Fig. 3 *A* and *B*, respectively. The OPD array comprises eight OPD pixels, where each OPD row contains two OPD pixels. Brown markers from darker to lighter shades are used to label rows 1–4 of the OPD array. The same markers are used to present the performance characteristics of the OPD pixels. As for the 2 × 2 red and NIR OLED arrays, rows 1 and 3 contain the four red OLED pixels, and rows 2 and 4 contain the four NIR OLED pixels. The ROA is formed by stacking the OLED and OPD arrays. The arrays are assembled such that emitter–detector spacing of 0.5 cm is maintained.

The performance parameters of the OPD array are shown in Fig. 3 *C–E*. The shade of brown lines indicates the row position of the pixels in the array as shown in Fig. 3*A*. An average EQE of 30% is observed across the absorption spectrum (Fig. 3*D*) with dark currents of a few nanoamperes per square centimeter (Fig. 3*C*). The cutoff frequency is mea-

sured at over 5 kHz for OPDs as shown in Fig. 3*E*. Since the operation frequency of the pulse oximeters is generally less than 1 kHz, this bandwidth is sufficient for oximetry. The linear dynamic response of the OPDs is shown in *SI Appendix, Fig. S7*.

The OLEDs show turn-on voltages at around 3 V as designated in the J-V characteristics in Fig. 3*F*. The OLEDs are operated at 10 mA·cm^{-2} for oximetry, where the red OLEDs provide 0.9 mW of flux, while the NIR OLEDs provide 0.2 mW of flux. The EQE values at operating conditions are ∼8–10% for red OLEDs and ∼2–3% for NIR OLEDs (Fig. 3*G*). The OLEDs demonstrate a change in performance parameters, depending on the row position due to the decrease in active layer thickness in the blade-coating direction; this variability can be mitigated by continuously feeding ink in front of the blade coater (15, 28). The variability in the OLED and OPD performance can be accommodated by taking a calibration measurement before using the array for oximetry. The emission spectrum of the OLEDs is shown in Fig. 3*H*, where the red OLED has a peak emission at 612 nm and the NIR OLED has a peak emission at 725 nm.

System Setup and Single-Pixel Reflection-Mode Pulse Oximetry. The full system implementation requires addressing individual pixels of the oximeter. Therefore, the hardware and software for the ROA are designed to support both single-pixel and array
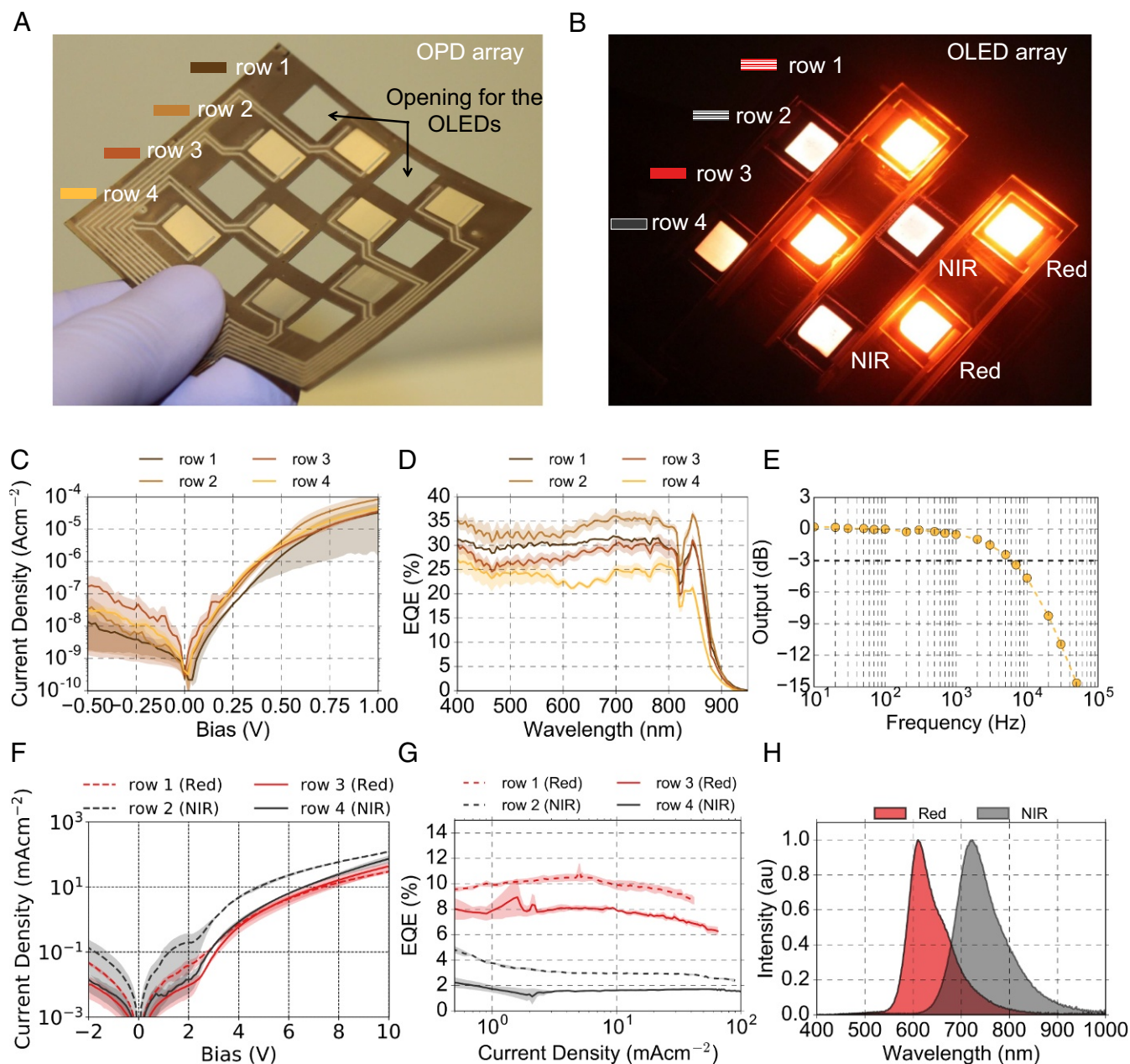
Fig. 3. Photographs and performance parameters of the OPD and OLED arrays. (*A*) OPD array composed of 8 pixels with 2 pixels in each row. The rows are marked using different shades of brown markers, which represent the legends of performance data presented in *C* and *D*. (*B*) Red and NIR OLED arrays: 2 × 2 red OLED array in rows 1 and 3 and 2 × 2 NIR OLED array in rows 2 and 4. The rows are marked using red and gray markers, which represent the legends of performance data presented in *F* and *G*. (*C*) Current density vs. voltage bias (*JV*) plot for the OPD array. Here each trace represents mean of the data in that row, while the shaded region shows the range of the data. (*D*) EQE of the OPD pixels in the array as denoted by row position in accordance with the colors in *A*. (*E*) The frequency response of an OPD pixel. The 3-dB cutoff is at over 5 kHz. (*F*) *JV* characteristics of the red and NIR OLED arrays as denoted by row position in accordance with the colors in *B*. (*G*) EQE as a function of current density of OLED arrays. (*H*) Emission spectra of the red and NIR OLED arrays.

measurements (Fig. 4*A*). The printed ROA is interfaced with the control electronics using flexible flat cable (FFC) connectors. Each pixel of the ROA is composed of one red and one NIR OLED and two OPDs. Signals from the red and NIR channels are read out sequentially using the two OPDs, and the average of the OPDs is used for signal processing. Using this format, the 4 × 4 device (OLEDs and OPDs) array provides 3 × 3 readout pixels. The pixels are selected using analog switches. An analog front end (AFE) sequentially drives the OLEDs and reads out the OPD signal. The AFE is controlled by a microcontroller. Software control of the AFE allows flexibility in choosing

OLED driving parameters and also gives access to the variable OPD gain circuitry. A photograph of the control electronics is shown in *SI Appendix*, Fig. S8, and the photographs of the software's graphical user interface (GUI) are shown in *SI Appendix*, Fig. S9.

To test the reflectance oximeter in the single-pixel mode, we used a setup where oxygenation of a volunteer can be changed by varying the oxygen concentration of the inhaled air (Fig. 4*B*). An altitude simulator is used to change the oxygen concentration of the air the volunteer breathes in via a facemask. Depending on the oxygen concentration of the air, the volunteer's
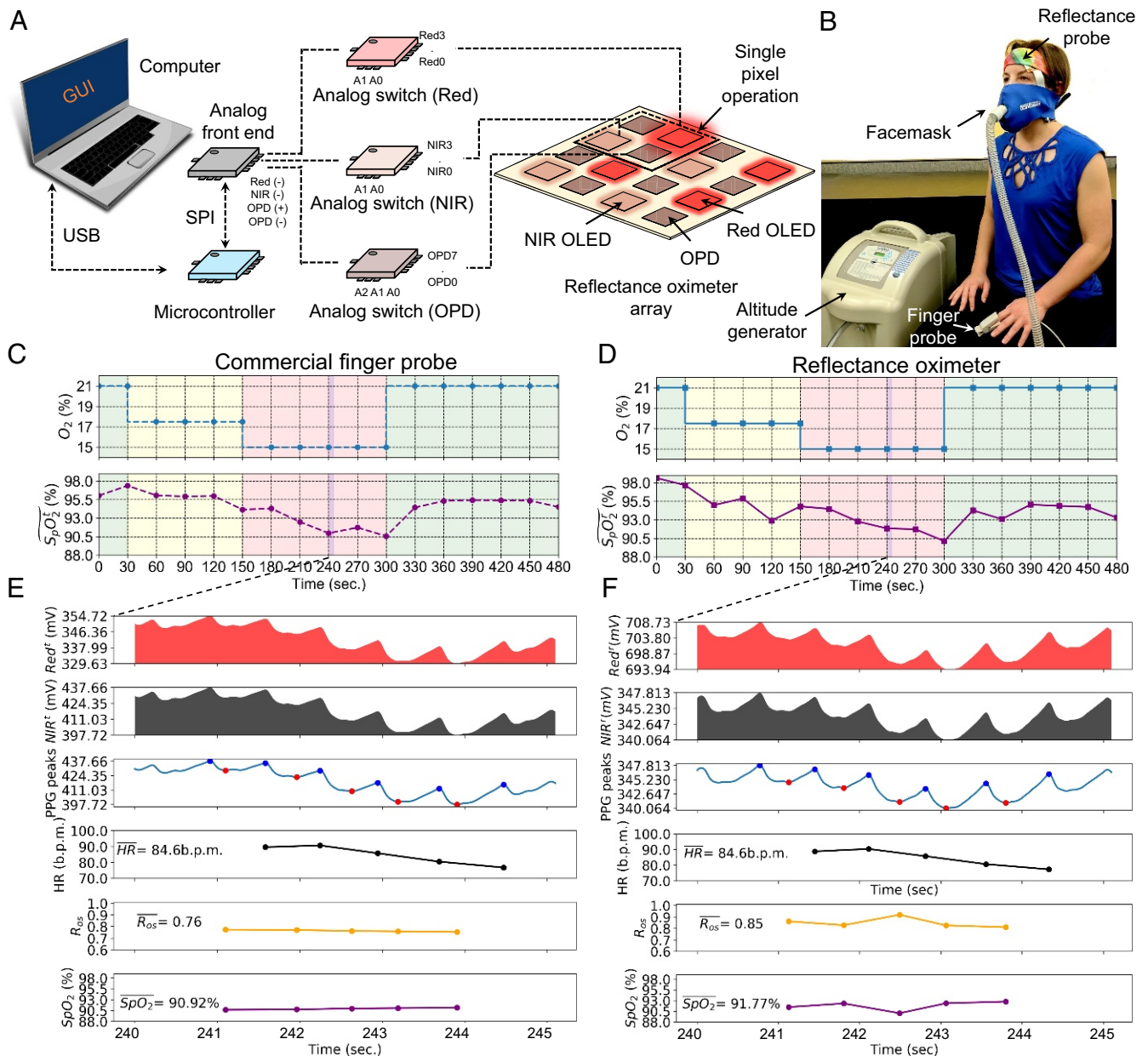
Fig. 4. System design for reflectance oximetry and single-pixel reflection-mode pulse oximetry (SpO_2^r) results. (*A*) Reflectance oximeter system design. Each pixel of the ROA (one red and one NIR OLED and two OPDs) is connected to an AFE using analog switches, for both single-pixel and array operation. The AFE drives the OLEDs and reads out the OPD signal. The AFE is controlled using an Arduino Due microcontroller. The data are then collected using a universal serial bus (USB) interface and processed using custom software. (*B*) Setup for changing oxygen saturation of human volunteers. An altitude simulator varies the oxygen content of the air the volunteer breathes in via a facemask. The SpO_2 is recorded using a commercial probe on the finger and the reflectance oximeter on the forehead. (*C* and *D*) Results from the commercial transmission-mode finger probe oximeter (SpO_2^t) and the reflectance oximeter (SpO_2^r), where the oxygen concentration is changed from 21% to 15%. Shown are the oxygen concentration of the air (*C* and *D*, *Top*, blue trace) and calculated oxygen saturation using SpO_2^t and SpO_2^r (*C* and *D*, *Bottom*, purple trace). (*E* and *F*) Zoomed-in data for the SpO_2^t in *C* and SpO_2^r in *D* during 240 s < t < 245 s show the red channel, NIR channel, PPG peaks, heart rate, R_{os}, and SpO_2.

oxygenation changes. This change in oxygenation is then picked up by a commercial finger probe sensor and using the reflection-mode sensor on the forehead. Calculated oxygen saturation using the commercial probe (SpO_2^t) and the reflectance probe (SpO_2^r) is shown in Fig. 4 *C* and *D*. We varied the inhaled oxygen concentration ($O_2\%$) from 21% to 15% over a period of 8 min. During the first 30 s, a baseline oxygen concentration of 21% was set and then reduced to 17.5% at $t = 30$ s; after keeping $O_2\%$ at 17.5% for 120 s, $O_2\%$ was further reduced to 15% at $t = 150$ s and was kept at that level for 150 s. Then $O_2\%$ was brought back to the baseline of 21%.

For the transmission-mode probe, oxygen saturation (SpO_2^t) drops from 96% to 90.5% and then comes back up to 94.5%. For the reflection-mode probe on the forehead, oxygen saturation (SpO_2^r) changes from 98% to 90.4% and then comes back up to 93.5%. We observed 1.1% mean error between SpO_2^t and SpO_2^r over the period of 8 min. The PPG signals for both transmission and reflection-mode probes at 240 s < t < 245 s are shown in Fig. 4 *E* and *F*. PPG signal peaks and calculated heart rate from the PPG peaks show almost identical results for both SpO_2^t and SpO_2^r. Here, an error of 0.85% is seen between SpO_2^t and SpO_2^r, which falls

within the 1% to 2% error margin that is inherent to pulse oximetry.

The pulse arrival times at the forehead and the fingers are different; the delay is on the order of 50 ms (29), which may slightly affect the pulse oxygenation calculations. Therefore, for a more direct comparison between the transmission- and reflection-mode pulse oximetry, we collected pulse oximetry data in both transmission and reflection mode from the fingers of the same hand as shown in *SI Appendix*, Fig. S10. In this experiment, the printed reflectance probe is placed under one finger and the commercial transmission-mode finger probe is worn on another finger. The commercial and reflectance finger probes provide almost identical SpO_2 variation with different concentrations of the inhaled oxygen. We observed a mean error of 0.41% between the commercial transmission-mode finger probe and the printed reflectance oximeter.

To investigate the temperature effects of the reflectance sensor, we operated the OLEDs of the device at different drive conditions and recorded the corresponding temperatures of the sensor on a volunteer's forearm (*SI Appendix*, Fig. S11). We observed a negligible change in the temperature—the sensor temperature remained within 32 ± 0.5 °C under the different OLED drive voltages from 0 V to 9 V. Moreover, to study the effect of an external pressure on the reflectance sensor, we collected reflection-mode signal with and without a 0.7-kPa external pressure (*SI Appendix*, Fig. S12A). With the external pressure, the signal baseline changes for both red and NIR channels, and the PPG ac signal magnitude improves for the red channel (*SI Appendix*, Fig. S12B) compared with the PPG ac signal without an external pressure (*SI Appendix*, Fig. S12C). However, for pulse oximetry calculations, the ratio of pulsatile (ac) to stationary (dc) signals at the two wavelengths is used, which remains almost the same: $R'_{os} = 0.65$ with external pressure, and $R'_{os} = 0.67$ without external pressure.

In Vivo 2D Oxygen Saturation Monitoring. The pulse oximetry model is applicable when there is a pulsatile arterial blood signal. In the absence of a pulsatile arterial blood signal, we use the modified model (Eq. 5 and *SI Appendix*) to monitor local changes in tissue oxygenation of a volunteer's arm under normal and ischemic conditions. By restricting blood supply to the arm with a pressure cuff, we induce temporary ischemia to the arm by inflating the pressure cuff to 50 mmHg over the systolic pressure. We use the ROA to monitor the change in oxygen saturation (ΔSO_2) under normal conditions and under pressure-cuff–induced ischemia with the ROA. The measurement setup is shown in Fig. 5A, where the ROA is used to measure ΔSO_2 on the forearm, while the pressure cuff is used to control blood supply to the arm, subsequently changing ΔSO_2 of the sensed tissue. Under normal conditions, there is a pulsatile arterial blood signal (*SI Appendix*, Fig. S13), which can be used with the pulse oximetry model. However, when the blood supply is restricted, only reflectance oximetry can be performed to measure ΔSO_2.

The 4×4 OLED and OPD devices provide 3×3 oximeter pixels. These pixels are indexed as pixels 1–9, (Px1–Px9) and are shown in Fig. 5B. A raster scan from Px1 to Px9 is used to collect data from the tissue. We used raster scanning speeds ranging from 100 ms·Px^{-1} to 1 s·Px^{-1}. Within this range, we did not observe analog-to-digital converter (ADC) channel leaking. For each pixel, samples are collected at 500 Hz, and then the collected data are averaged. At a sampling rate faster than 50 ms·Px^{-1}, we observed ADC channel leaking. The limiting factors to achieve a faster scanning speed are the 3-dB cutoff of the OPDs, the resistance and capacitance associated with each channel, and the settling time of the analog switches. After collecting data from all 9 pixels, 2D contour maps of red and NIR channels and ΔSO_2 are created. For the in vivo 2D oxygen saturation monitoring test, data during the first 30 s are collected under normal conditions and are considered the baseline. The pressure cuff is then used to induce ischemia; therefore the signal amplitude in the red and NIR signal channels gradually decreases. Once the pressure is released, the signals overshoot, going over the baseline (Fig. 5C). Fig. 5D shows the 2D maps of red and NIR signal channels and ΔSO_2 during the test under normal conditions ($t = 0$ s), under ischemia ($t = 60, 120$ s), and after releasing the pressure cuff ($t = 180, 240, 300$ s). Since this is a transient measurement, ΔSO_2 remains at the baseline ($\Delta SO_2 = 0\%$) at $t = 0$ s, under ischemia ΔSO_2 drops to -9.3% at $t = 150$ s, and after releasing the pressure cuff ΔSO_2 increases to $+8.4\%$ at $t = 180$ s and comes back to the baseline $+0.7\%$ at $t = 300$ s. The 2D contour maps at every 30-s interval are provided in *SI Appendix*, Fig. S14. We also monitored how different durations of ischemia affect ΔSO_2. *SI Appendix*, Fig. S15 provides ΔSO_2 monitoring for 1 min, 2 min, and 2.5 min of ischemia, and ΔSO_2 drops to -6%, -9.5%, and -11.3%, respectively, during these experiments. The results obtained in these tests agree with the studies reported in the literature on pressure-cuff–induced ischemia (20, 24, 30, 31).

In the 2D oxygenation mapping experiments, we monitored tissue oxygenation of the forearm with and without pressure-cuff–induced ischemia. When blood supply to the arm is occluded using the pressure cuff, oxygenated blood cannot circulate to the forearm, which results in a drop in tissue oxygenation. We recorded this change in oxygenation using the ROA. With the status quo, i.e., transmission-mode pulse oximetry, this change in oxygenation cannot be observed, because when blood circulation is cut off, the pulsatile arterial blood signal disappears, which is essential to calculate the pulse oxygenation using transmission-mode pulse oximetry. The ROA can measure the change in SO_2. Moreover, with the 2D mapping capability, the ROA can monitor oxygenation of an area rather than a single point, which is promising for monitoring oxygenation of tissues, wounds, and newly transplanted organs. In addition, the ROA can be integrated to a multimodal near-infrared spectroscopy (NIRS) system, where the ROA is interfaced to printed electromyography (EMG) or electrocardiography (ECG) electrodes on a flexible substrate to provide a lightweight, comfortable, and wearable sensor platform for muscle assessment during a person's normal activities and exercise (32–34).

Discussion

Existing techniques for measuring oxygen concentration in blood heavily rely on noninvasive transmission-mode pulse oximetry (SpO_2^t), which presents two fundamental limitations: (*i*) Sensing locations are limited to only tissues that can be transilluminated and (*ii*) only single-point measurements can be performed with SpO_2^t due to the sensor configuration. Here, we presented a flexible and printed electronic system realized by printing and integrating arrays of organic optoelectronics for measuring oxygen saturation in the reflection mode. Two different modes of oximeter operations are discussed: (*i*) reflection-mode pulse oximetry (SpO_2^r), when pulsatile PPG signal is present, and (*ii*) reflectance oximetry, when pulsatile PPG signal is absent. Additionally, we explored the sensor design and placement of the sensor on the body. The forehead provided the strongest pulsatile signal. By using the reflectance oximeter, we monitored oxygen saturation of a volunteer on the forehead and successfully measured SpO_2^r with a mean error of 1.1%. The use of an altitude simulator to change the oxygen concentration verified the efficacy of the reflectance oximeter under both hypoxia and normal conditions. Finally, in the case of a medical shock, low blood perfusion, or locations on the body with a low PPG signal, we demonstrate a method to determine ΔSO_2 in the absence of a pulsatile
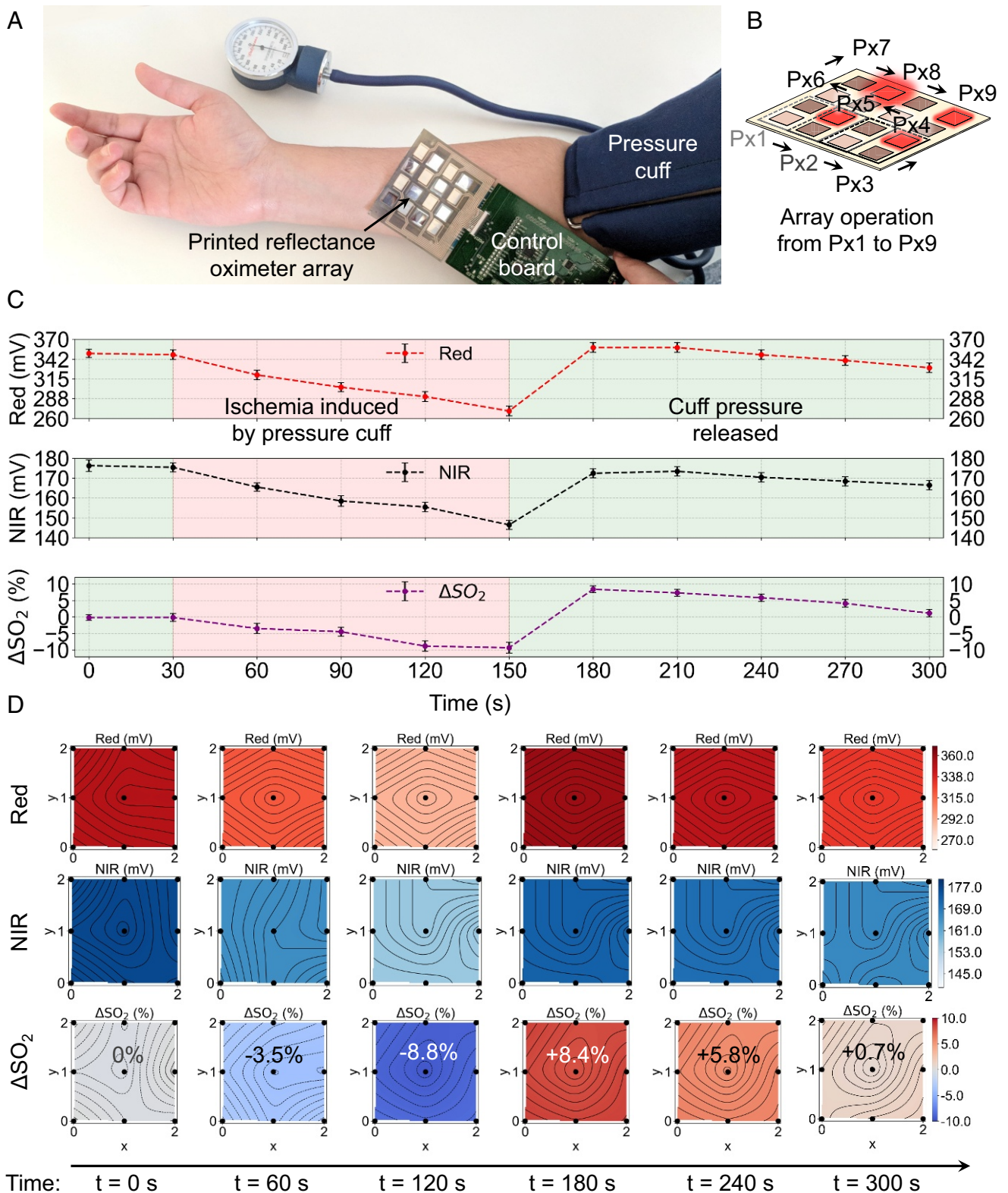
Fig. 5. In vivo 2D oxygen saturation monitoring with the ROA. (*A*) The ROA is placed on a volunteer's forearm to monitor the change in oxygen saturation (ΔSO_2). Blood supply to the forearm is controlled by a pressure cuff. The 4×4 devices of the ROA provide 3×3 oximeter pixels. (*B*) Oximeter pixel switching during the array operation. Each pixel is composed of one red and one NIR OLED and two OPDs. A raster scan from pixel 1 (Px1) to pixel 9 (Px9) is used to collect data from the tissue. (*C*) ΔSO_2 for pressure-cuff–induced ischemia for a recording of 300 s. Red, NIR, and ΔSO_2 data are shown as red, black, and purple dotted lines (dotted lines represent the means of the nine oximeter pixels, and error bars represent the SD of the data). Using the pressure cuff, blood supply to the forearm is occluded and restored. In the first 30 s, a baseline reading with no ischemia is taken. The pressure cuff is then inflated to 50 mmHg over the systolic pressure at 30 s $< t <$ 150 s and released at $t = 150$ s. ΔSO_2 varies from 0% under normal conditions to -9.3% ($t = 150$ s) under ischemia and to $+8.4\%$ ($t = 180$ s) immediately after releasing the pressure cuff. (*D*) Two-dimensional contour maps of red, NIR, and ΔSO_2 under normal conditions ($t = 0$ s), under ischemia ($t = 60, 120$ s), and after releasing the pressure cuff ($t = 180, 240, 300$ s).

blood signal. The ROA was used to spatially map oxygenation values of a volunteer's forearm under normal and ischemic conditions.

Flexible organic and inorganic optoelectronics enhance the SNR of oximetry by reducing the ambient noise signal. Our demonstration of the ROA in this paper increases the sensing locations of oximetry and enables measuring oxygenation in the absence of pulsatile arterial blood signal. Additionally, the use of printing techniques such as blade coating and screen printing to fabricate the sensor on flexible plastic substrates makes the sensor both comfortable to wear and efficient at extracting high-quality biosignal. This work presented an unprecedented level of control and integration in printed electronic systems. We hope that our demonstration of the flexible reflection oximeter array with 2D spatial mapping capability will encourage novel sensing schemes and aid in medical sensing applications such as 2D mapping of oxygenation in tissues, skin grafts, wounds, and transplanted organs.

Materials and Methods

Fabrication and Characterization of the OLED Arrays. The OLED arrays were printed on 125-μm thick ITO patterned PEN substrates. Two 1-cm wide ITO strips were placed 1.1 cm apart from each other, for creating the two columns of the OLEDs. The substrate was placed on a hotplate at 80 °C for 3 h under vacuum. The sample was then taken out in the air and placed on a hotplate at 180 °C for 1 h. Then the substrate was treated with plasma for 10 s and the entire surface was treated with (heptadecafluoro1,1,2,2-tetrahydrodecyl) (Gelest SIH5841.0) for 20 min under light vacuum (0.1–1 Torr) to make the surface hydrophobic. The treated substrate was kept in a nitrogen-filled chamber overnight. The substrate was patterned, exposing the active area of the OLEDs by using plasma to selectively etch off the hydrophobic layer. Then PEDOT:PSS (Clevios AI4083; Heraeus), the interlayer, and the semiconducting polymers (Cambridge Display Technologies Ltd.) were subsequently blade coated to form the emissive layer of the OLEDs. Concentrations of 6 mg·mL^{-1} and 20 mg·mL^{-1}, respectively, were used for the interlayer and the emissive layer. After all of the layers were blade coated, the samples were taken out of the glovebox for screen printing. After the dielectric and the silver traces were screen printed, the samples were transferred to a thermal evaporator in a glovebox to evaporate calcium (99.5%; Strem Chemicals) and aluminum (99.999%; ACI Alloys) to finish the OLED stack. The final device stack consisted of 70 nm PEDOT:PSS, 100 nm OLED emissive layer, 10 nm calcium, and 100 nm aluminum. Each pixel was encapsulated by face sealing using a UV curable epoxy (Delo Katiobond LP612) and plastic film (PQA1) on top. A power source unit (Keithley 2600) was used to sweep voltage across the devices and an integrating sphere (Orb Optronix SP-75 spectrometer) was used to measure flux out of the OLEDs.

Fabrication and Characterization of the OPD Array. The OPD array was printed on top of planarized PEN substrates (TeiJin PQA1), using blade-coating techniques. The substrate was first plasma treated in Tegal Plasmod at 50 W for 10 s. The substrate was then placed in a vacuum with 40 μL of heptadecaflouropolymer for 20 min to render the substrate hydrophobic. A stainless steel stencil with cutouts of the desired PEDOT:PSS area was placed on top of the substrate and then treated for 1.2 min with oxygen plasma in a Diener Nano plasma system. A total of 30 μL of PEDOT:PSS was dispensed uniformly in front of the blade. Then ink was blade coated with a blade height of 100 μm and speed of 1 cm·s^{-1}. The substrate was then annealed for 10 min at 120 °C. The substrate was then plasma treated in

Tegal Plasmod at 50 W for 10 s. A total of 50 μL of 1:2 CDT Donor:PC71BM in 95:5 3,3′,5,5′-tetramethylbenzidine:benzyl benzoate (TMB:BB) was dispensed at the top of the array. Then ink was blade coated with a blade height of 200 μm and speed of 2.5 cm·s^{-1}. The substrate was then annealed for 1.5 h at 120 °C. Next, silver flake paste was screen printed on top of the array and then annealed in a glove box for 5 min at 120 °C. Finally, an aluminum cathode at a base pressure of $5 \cdot 10^{-6}$ Torr at a rate of 3–5 Å·s^{-1} was evaporated to finish the OPD stack. The final device stack consisted of 50 nm PEDOT:PSS, 150 nm OPD active layer, and 60 nm aluminum.

Control Electronics for the ROA. The control electronics were designed to support reflectance oximetry in the single-pixel and the array mode. Additionally, the system was designed to measure oxygenation with or without the pulsatile arterial blood signal. We used a Texas Instruments AFE (AFE4490) to sequentially drive the OLEDs and read out the OPD signal. The OLED and OPD arrays were interfaced with the control electronics using FFC connectors. The pixels in the array were selected using analog switches (Analog Devices ADG1608). The AFE was controlled with an Arduino Due microcontroller. Software control of the AFE allowed flexibility in choosing OLED driving parameters and allowed adjustments to the variable OPD gain circuitry. The OLEDs were driven at 10 mA·cm^{-2} with a 9-V battery in push–pull mode. A two-stage OPD gain circuitry was used to amplify the photocurrent. A 100-kΩ feedback resistor was used in the first stage, and unity gain was used in the second stage. Finally, the data were collected using a USB interface and were processed using custom in-house software.

Reflection-Mode Pulse Oximetry (SpO_2^r) Data Collection and Processing. For monitoring oxygenation in the presence of a pulsatile signal, the oxygenation of the volunteer was changed by using an altitude simulator (Everest Summit II Altitude Generator). Altitudes of 5,000 feet and 8,000 feet correspond to oxygen concentrations of 17.5% and 15%, respectively. The change in oxygen concentration changed oxygen saturation of the volunteer, which was monitored using a transmission-mode oximeter probe on the finger (SpO_2^t) and the printed reflectance probe on the forehead (SpO_2^r). Data for the red and NIR channels were collected for both SpO_2^t and SpO_2^r simultaneously, using the control electronics. PPG peaks, heart rate, and the ratio of the ratios of the red and NIR PPG signals were calculated, and then a modified Beer–Lambert's law (Eq. 2) in addition to an empirical correction was used to calculate both SpO_2^t and SpO_2^r.

Reflectance Oximetry Data Collection and Processing. For measuring oxygenation in the absence of a pulsatile arterial blood signal, forearm ischemia was induced in human volunteers, using a pressure cuff. After taking a baseline measurement, the pressure cuff was used to induce ischemia, using a pressure of 50 mmHg over the systolic pressure. The cuff was released after 2 min of ischemia. Data were recorded for 5 min to observe the change in oxygenation using the ROA. A raster scan from Px1 to Px9 was used to collect data from the tissue. A modified model as described in Eq. 5 was used to monitor oxygenation of tissue. Data from the 9 pixels were plotted using nearest-neighbor interpolation to create the 2D spatial maps of red and NIR channels and the change in oxygenation.

All reflectance oximetry experiments performed on human subjects were carried out with informed consent under the approval of the University of California, Berkeley Institutional Review Board, protocol ID 2014-03-6081.

1. Webster JG (1997) *Design of Pulse Oximeters* (Taylor & Francis, New York).
2. Nakajimi S, Hirai H, Takase H, Kuze A, Aoyagi S (1975) [New pulsed-type earpiece oximeter]. *Respiration Circ* 23:709–713. Japanese.
3. Someya T, Bao Z, Malliaras GG (2016) The rise of plastic bioelectronics. *Nature* 540:379–385.
4. Choi S, Lee H, Ghaffari R, Hyeon T, Kim DH (2016) Recent advances in flexible and stretchable bio-electronic devices integrated with nanomaterials. *Adv Mater* 28:4203–4218.
5. Trung TQ, Lee NE (2016) Flexible and stretchable physical sensor integrated platforms for wearable human-activity monitoring and personal healthcare. *Adv Mater* 28:4338–4372.
6. Fang H, et al. (2017) Capacitively coupled arrays of multiplexed flexible silicon transistors for long-term cardiac electrophysiology. *Nat Biomed Eng* 1:0038.
7. Lu C, et al. (2017) Flexible and stretchable nanowire-coated fibers for optoelectronic probing of spinal cord circuits. *Sci Adv* 3:e1600955.
8. Gao W, et al. (2016) Fully integrated wearable sensor arrays for multiplexed in situ perspiration analysis. *Nature* 529:509.
9. Lee JW, et al. (2016) Soft, thin skin-mounted power management systems and their use in wireless thermography. *Proc Natl Acad Sci USA* 113:6131–6136.
10. Kabiri Ameri S, et al. (2017) Graphene electronic tattoo sensors. *ACS Nano* 11:7634–7641.
11. Tee BCK, et al. (2015) A skin-inspired organic digital mechanoreceptor. *Science* 350:313–316.
12. Kim J, et al. (2016) Battery-free, stretchable optoelectronic systems for wireless optical characterization of the skin. *Sci Adv* 2:1600418.
13. Yokota T, et al. (2016) Ultraflexible organic photonic skin. *Sci Adv* 2:e1501856.

ENGINEERING

MEDICAL SCIENCES

14. Kim J, et al. (2017) Miniaturized battery-free wireless systems for wearable pulse oximetry. *Adv Funct Mater* 27:1604373.

15. Han D, et al. (2017) Flexible blade-coated multicolor polymer light-emitting diodes for optoelectronic sensors. *Adv Mater* 29:1606206.

16. Bansal AK, Hou S, Kulyk O, Bowman EM, Samuel ID (2015) Wearable organic optoelectronic sensors for medicine. *Adv Mater* 27:7638–7644.

17. Lochner CM, Khan Y, Pierre A, Arias AC (2014) All-organic optoelectronic sensor for pulse oximetry. *Nat Commun* 5:5745.

18. Haahr RG, et al. (2012) An electronic patch for wearable health monitoring by reflectance pulse oximetry. *IEEE Trans Biomed Circuits Syst* 6:45–53.

19. Sen CK (2009) Wound healing essentials: Let there be oxygen. *Wound Repair Regen* 17:1–18.

20. Boas DA, Franceschini MA (2011) Haemoglobin oxygen saturation as a biomarker: The problem and a solution. *Philos Trans R Soc A* 369:4407–4424.

21. Ericson M, et al. (2004) Implantable sensor for blood flow monitoring after transplant surgery. *Minimally Invasive Ther Allied Tech* 13:87–94.

22. Yudovsky D, Pilon L, Nouvong A, Schomacker K (2011) Assessing diabetic foot ulcer development risk with hyperspectral tissue oximetry. *J Biomed Opt* 16:026009.

23. Atchley DW (1930) Medical shock. *J Am Med Assoc* 95:385–389.

24. Duncan A, et al. (1995) Optical pathlength measurements on adult head, calf and forearm and the head of the newborn infant using phase resolved optical spectroscopy. *Phys Med Biol* 40:295–304.

25. Han D, Khan Y, Gopalan K, Pierre A, Arias AC (2018) Emission area patterning of organic light-emitting diodes (OLEDs) via printed dielectric. *Advanced Functional Materials* 28:1802986.

26. Pierre A, Deckman I, Lechêne PB, Arias AC (2015) High detectivity all-printed organic photodiodes. *Adv Mater* 27:6411–6417.

27. Pierre A, et al. (2014) All-printed flexible organic transistors enabled by surface tension-guided blade coating. *Adv Mater* 26:5722–5727.

28. Shin S, Yang M, Guo LJ, Youn H (2013) Roll-to-roll cohesive, coated, flexible, high-efficiency polymer light-emitting diodes utilizing ITO-free polymer anodes. *Small* 9:4036–4044.

29. Lázaro J, et al. (2016) Difference in pulse arrival time at forehead and at finger as a surrogate of pulse transit time. *2016 Computing in Cardiology Conference (CinC)* (IEEE, Piscataway, NJ), pp 269–272.

30. Hampson NB, Piantadosi CA (1988) Near infrared monitoring of human skeletal muscle oxygenation during forearm ischemia. *J Appl Physiol* 64:2449–2457.

31. Wariar R, Gaffke JN, Haller RG, Bertocci LA (2000) A modular NIRS system for clinical measurement of impaired skeletal muscle oxygenation. *J Appl Physiol* 88:315–325.

32. Hu G, Zhang Q, Ivkovic V, Strangman GE (2016) Ambulatory diffuse optical tomography and multimodality physiological monitoring system for muscle and exercise applications. *J Biomed Opt* 21:091314.

33. Poliks M, et al. (2016) A wearable flexible hybrid electronics ECG monitor. *2016 IEEE 66th Electronic Components and Technology Conference (ECTC)* (IEEE, Piscataway, NJ), pp 1623–1631.

34. Moin A, et al. (2018) An EMG gesture recognition system with flexible high-density sensors and brain-inspired high-dimensional classifier. *2018 IEEE International Symposium on Circuits and Systems (ISCAS)* (IEEE, Piscataway, NJ), pp 1–5.